HAL open science

In situ plant materials hyperspectral imaging by multimodal scattering near-field optical microscopy

Anne Charrier, Aubin C Normand, Ali Passian, Philip Schaefer, Aude L. L. Lereu

To cite this version:

Anne Charrier, Aubin C Normand, Ali Passian, Philip Schaefer, Aude L. L. Lereu. In situ plant materials hyperspectral imaging by multimodal scattering near-field optical microscopy. Communications Materials, 2021, 2, pp.59. 10.1038/s43246-021-00166-7 . hal-03287592

HAL Id: hal-03287592

https://hal.science/hal-03287592

Submitted on 15 Jul 2021

HAL is a multi-disciplinary open access archive for the deposit and dissemination of scientific research documents, whether they are published or not. The documents may come from teaching and research institutions in France or abroad, or from public or private research centers.

L'archive ouverte pluridisciplinaire **HAL**, est destinée au dépôt et à la diffusion de documents scientifiques de niveau recherche, publiés ou non, émanant des établissements d'enseignement et de recherche français ou étrangers, des laboratoires publics ou privés.

communications materials

ARTICLE

https://doi.org/10.1038/s43246-021-00166-7 OPEN

In situ plant materials hyperspectral imaging by multimodal scattering near-field optical microscopy

Anne M. Charrier [1], Aubin C. Normand[1,2], Ali Passian [3], Philip Schaefer[4] & Aude L. Lereu [2]✉

Plant cells are elaborate three-dimensional polymer nano-constructs with complex chemistry. The bulk response of plants to light, in the far-field, is ultimately encoded by optical scattering from these nano-constructs. Their chemical and physical properties may be acquired through their interaction with a modulated nano-tip using scattering scanning near-field optical microscopy. Here, using this technique, we present 20 nm spatial resolution mechanical, spectral and optical mappings of plant cell walls. We first address the problem of plant polymers tracking through pretreatment and processing. Specifically, cellulose and lignin footprints are traced within a set of delignified specimen, establishing the factors hindering complete removal of lignin, an important industrial polymer. Furthermore, we determine the frequency dependent dielectric function $\epsilon(\omega) = (n + ik)^2$ of plant material in the range $28 \leq \omega \leq 58$ THz, and show how the environmental chemical variation is imprinted in the nanoscale variability of n and k. This nanometrology is a promise for further progress in the development of plant-based (meta-)materials.

[1] Aix Marseille Univ, CNRS, CINaM, Marseille, France. [2] Aix Marseille Univ, CNRS, Centrale Marseille, Institut Fresnel, Marseille, France. [3] Oak Ridge National Laboratory, Oak Ridge, TN, USA. [4] Neaspec GmbH, Munich, Germany. ✉email: aude.lereu@fresnel.fr

Plants, a natural, ecological, and renewable resource, are widely exploited either in their raw state as building materials, in a composite state for the paper industry[1], or in a processed state in biofuels[2] and bioplastics[3,4]. As a class of biomaterials, it is very attractive for its mechanical, chemical, thermal, and more recently, optical properties[4–6]. However, owing to their organic nature, plant-derived materials are susceptible to degradation by microorganisms, fungi, and humidity. Therefore, a major concern, in for example wood industry, is to overcome or manage biodegradability and instability by developing chemical and/or physical treatments; among them: biocidal, thermal[7–9], surface functionalization of nanoparticles inclusions[10,11]. In the context of biofuel or pulp production, physical treatments are also developed to improve the cellulose yield, for example, by generating tension wood[12]. Such treatments induce local surface and subsurface modifications of the chemical composition of the plant cell walls (PCWs), hence affecting their physical and morphological properties. Molecular scale monitoring is, therefore, necessary to observe, understand, and control these changes, and to question: "How do the chemical variations impact the physical properties (mechanical, hygroscopic, thermal and, as discussed here, optical) at the nanoscale?" and "How are these changes distributed within the heterogeneity of PCWs?" or "How can the altered physical properties impact the wood industry?". These questions are still largely open despite the recent progress in spectroscopically probing the materials at length scales akin to the molecular distributions[13]. This work explores the chemical and optical properties of PCWs at the molecular scale, a heretofore-largely uncharted material domain. To access the nanoscale, atomic force microscopy (AFM)-based techniques have been utilized to study PCW structures and their nanomechanical properties (e.g., elastic modulus and viscoplasticity); for example, during the aging of flax fibers[14], during delignification[15,16], or to investigate starch granules functionality[17]. However, the chemical information and optical properties are currently inaccessible at the scale of the cell wall constituents.

Nano-optical properties of plant biomaterials are of increasing interest. At present, there is a major interest in developing transparent papers as flexible and biodegradable substrates with high optical, mechanical, and thermal performances for green electronics and optics[4]. In this trend, Wu et al.[6] investigated the action of delignification treatment to produce transparent wood while keeping a certain level of mechanical properties. More recently, Orelma et al.[18] have made plant cellulose-based optical fibers in the visible-near infrared (IR) range with an attenuation of 6.3 dB/cm at 1300 nm. Here, again, physical treatments and chemical extractions are implemented to explore the physical, chemical, and morphological properties of biomass toward creating biodegradable and biocompatible optical components. Optical studies to date have been based on extracting lignin or cellulose by ellipsometry or reflectometry measurements[19]. In this trend, scanning near-field optical microscopy (SNOM) has been reported as the tool of choice[20–22]. However, the used aperture-SNOM is limited to imaging in the visible spectrum, where the optical signal (either reflectivity or transmission) is recorded at each position of the scanned region through a fiber-probe[23–25]. The spatial resolution reported in these studies has the upper limit set by the achievable resolution of aperture-SNOM, that is, ~100 nm. Furthermore, the fiber-based aperture-SNOM is not amenable to spectroscopy in the IR spectrum, where the fingerprint of the major constituents of PCWs is found (see Methods section). Given the limited spatial resolution and spectral IR-incompatibility of SNOM, only lower resolution reflectivity measurements of PCW under monochromatic visible light have been reported. Therefore, the acquisition of the nanospectroscopic data and the nanoscale optical dielectric function of in situ PCWs remains in demand.

Similarly, much efforts are underway to determine and exploit the chemical composition of biomaterials. Consequently, attempts to acquire chemical information with a resolution typically in the range ~10–300 nm, have been reported based on techniques such as interference microscopy[19], micro- or attenuated total reflectance Fourier transform IR[26–32], and micro-Raman[33–37] spectroscopies, including their confocal counterparts. However, thus far, reports have been insufficient to devise access to the scale of the wood constituents and to correlate chemistry to physical properties. Tip-based techniques, beating the diffraction limit, are emerging as the most promising spectroscopic measurement modalities. These methods typically capitalize upon the local interaction of light with the nanoscale apex of a tip and the subtended sample surface. The combined tip-specimen dynamical system and its interaction with an incident field provide a platform where nanomechanics meets nano-optics. An example is the exploratory system of hybrid photonics-nanomechanical force microscopy (HPFM)[38], in which, nonlinear tip-sample interactions and the ensuing frequency mixing are utilized in conjunction with an amplitude modulated tunable IR laser beam. Although HPFM has been demonstrated to provide excellent contrast related to nanoscale (~5–10 nm resolution) surface and subsurface chemical and morphological features, challenges in automation and proper calibration must be addressed in its further development before widespread use can be expected.

To advance the state of plant material nanometrology, tip-assisted IR scattering in the near field is described and to the best of our knowledge, the highest resolution PCW characterization is reported. The recently developed tip-based modality of s-SNOM, has demonstrated chemical mapping at spatial resolutions down to ~10 nanometers[39,40]. This new field has been evolving to allow hyperspectral imaging that enables studies of chemical distribution and composition even in low contrast polymer samples[41]. The information obtained from both the imaging and spectroscopy modes may be used for the simultaneous extraction of topography, mechanical phase, and optical amplitude and phase. The latter two are related to optical reflectivity and absorption of materials, which are directly linked to the nanoscale dielectric properties of the specimen[42]. The mechanical phase has been shown to be sensitive to the viscosity of the materials in relation to their chemical composition[43]. Here, multimodal s-SNOM is shown to answer specific questions related to the properties of PCWs at the nanoscale by correlating the local optical, chemical, and mechanical properties with a lateral resolution of 20 nm. The study focuses on PCWs of young poplar trees as it is widely used for biomass production and more specifically on the compositional distribution of lignin and cellulose, two of the most important polymers in wood cell walls. Using the IR absorption signal, the relative composition of the wood constituents can be extracted in situ without any fluorescent tagging or labeling. We describe an effective method to identify the wood modification under physical, biological, or chemical treatment. By determining the chemical distribution and the local values of the dielectric functions for both lignin and cellulose, we investigate the efficiency of a delignification process developed for biomass extraction. The guideline of this manuscript through the different s-SNOM modes used to trace the different physicochemical properties is outlined in the workflow Fig. 1.

Results and discussions

Multimodal s-SNOM for PCW studies. In s-SNOM, in contrast to diffraction-limited techniques, the spatial resolution is no

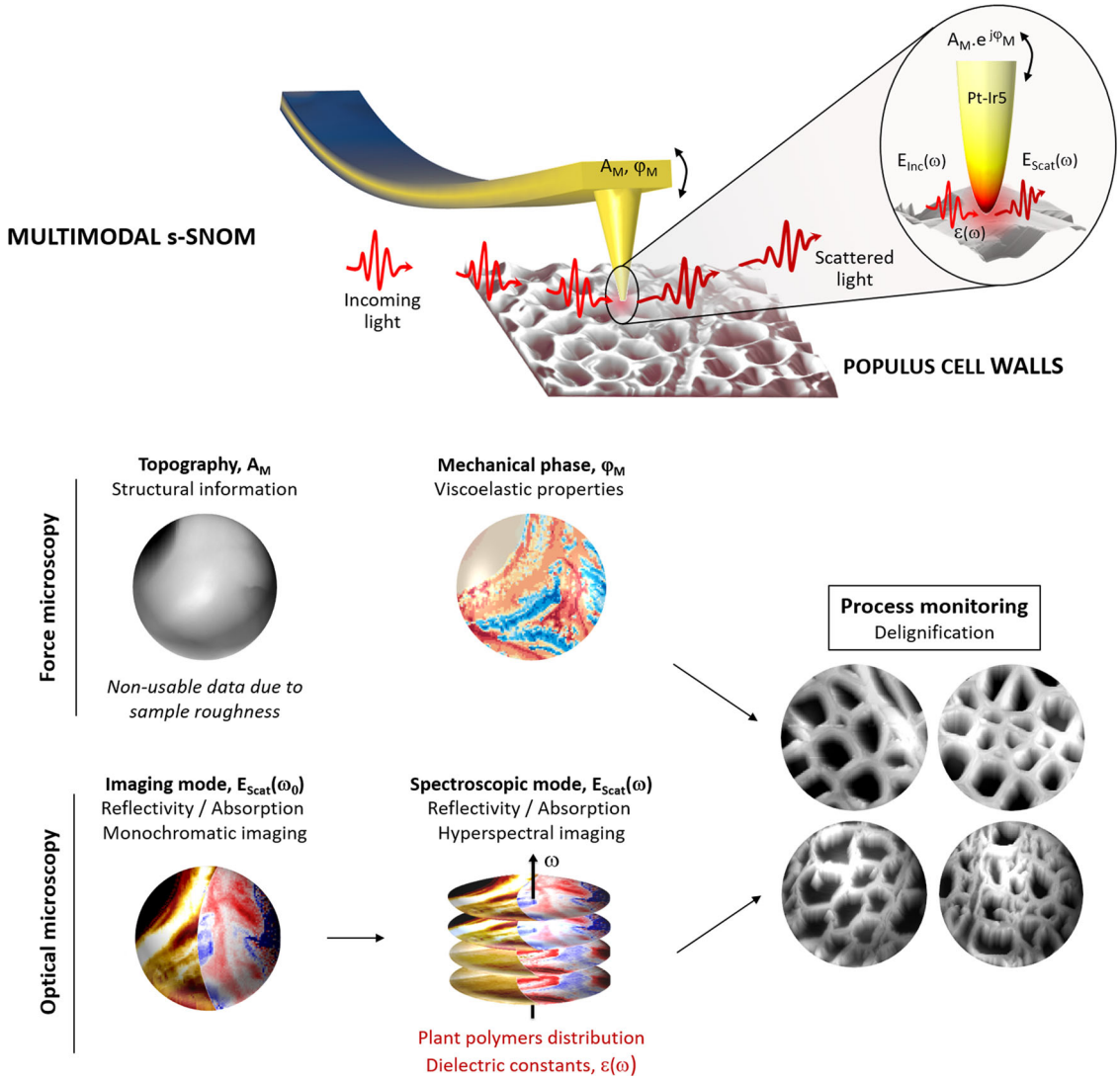

Fig. 1 The near-field region of a tip-cell walls system carries information on the chemical and dielectric properties of the specimen. The s-SNOM signal is based on the analysis of the scattered radiation detected in the far-field region. Shown is the microcantilever tip (oscillation amplitude A_M and phase φ_M) engaging the PCW surface while interacting with incoming radiation pulses E_{Inc}. The scattered field E_{Scat} is then detected and analyzed for its amplitude A_{Scat} and phase φ_{Scat}. These constants extracted from the tip-sample interaction are used in each mode to trace structural (topography, A_M), mechanical (mechanical phase, φ_M), and optical (reflectivity and absorption, A_{Scat}, φ_{Scat}) information. The color contrast in the cantilever and the tip represents computed stress distribution and surface field magnitude, respectively.

longer limited by the excitation wavelength of the incident light. Instead, it is a function of the size, geometric shape, and material of a probe tip. That is in contrast with topography acquisition for which the resolution is given by the convolution between the tip shape and size, and the sample roughness. In polymeric or other low optically contrasted materials, the tips need to be coated with metal to enhance the optical field at their apex, hence limiting the lateral resolution. In our case, the tips, coated with Pt-Ir5, have a curvature of 20 nm giving the lowest optical lateral resolution achievable with those tips. A higher resolution could be reached by reducing the tip curvature, as demonstrated in model samples[44]. Indeed, the s-SNOM probe tip acts as a nano-antenna when interacting with an incident light, as depicted in Fig. 1. This leads to an enhancement of the light near the tip apex, which is a strong nearfield created in a nanoscale volume under the tip. When the tip is in the nanoscale vicinity of a sample, the ensuing scattering alters when the tip moves across the sample surface and/or when the wavelength of the incident light changes. By collecting the tip-sample scattered light E_{Scat}, the sample optical response can be extracted from $I = |E_{Scat} + E_{Ref}|^2$, where E_{Ref} is a reference field[25,42], acquired over a known, highly reflective substrate (here silicon on glass, Supplementary Note 1 and Fig. 1) with small spectral variations over the employed wavenumber range. Background radiation due to scattering from the micro-cantilever shank, as well as from the comparatively large sample illumination, can compromise the signal. To suppress this background contribution, it is possible to guide the signal detection by exploiting the modulation frequencies of the cantilever. Indeed, in "tapping mode AFM", one drives the cantilever into oscillation. Therefore, working with second harmonic demodulation of the oscillation combined with pseudo-heterodyne detection[45,46], it is possible to achieve sufficient noise rejection. Thus, both the mechanical amplitude and phase of the cantilever oscillations as well as the optical amplitude and phase of the collected scattered light can be detected. This allows the simultaneous acquisition of topography, mechanical phase, and optical signals (reflectivity

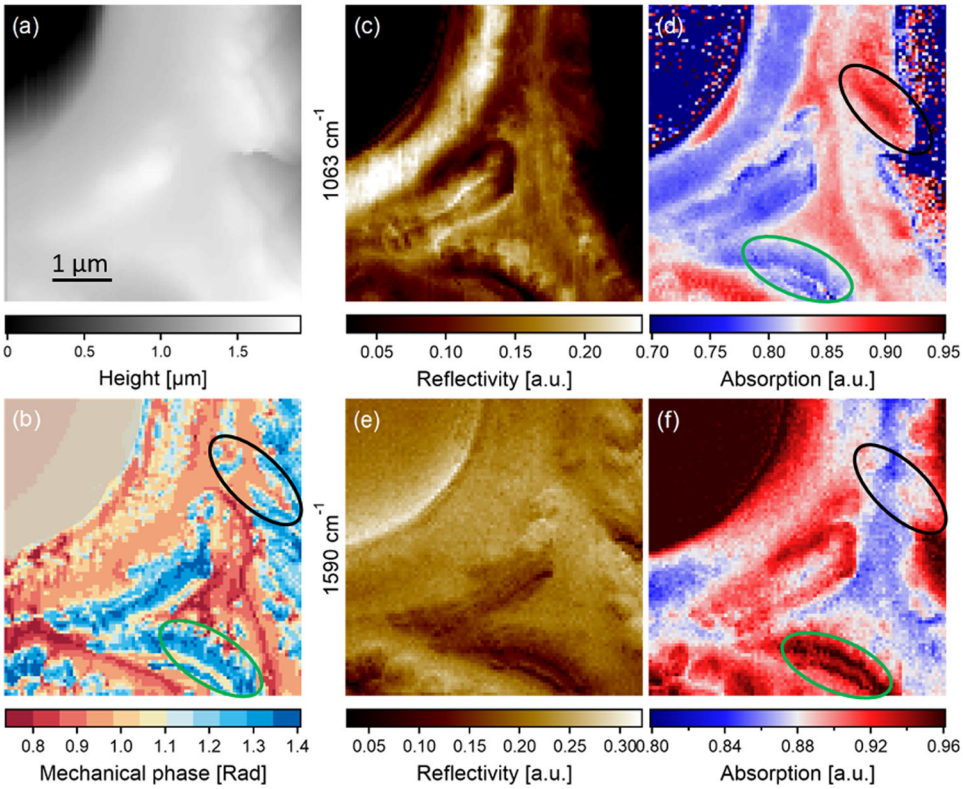

Fig. 2 Nanomechanical and nanospectroscopic imaging of PCWs. Results are shown for measurements on a 5 × 5 µm^2 region of a poplar cross-section. The signals comprise topography (**a**), mechanical phase (**b**), normalized reflectivity (**c** and **e**), and normalized IR absorption (**d** and **f**) at specific spectral peaks of cellulose (1063 cm^{-1}) and lignin (1590 cm^{-1}). The black and green ovals mark cellulose and lignin-rich regions, respectively, and highlight the correlation between the mechanical phase and the IR absorption mappings.

and absorption) of the investigated sample region. Imaging plant materials using tip-scattered near-field microscopy has been only recently reported in a study of pit membrane composition of *Populus Nigra* wood[47]. In an earlier study based on HPFM, a proof-of-principle chemical imaging of poplar cell walls has also been reported[38]. Here, employing the scattering-type SNOM (Neaspec GmbH) as depicted in Fig. 1, we report the highest resolution, nondestructive, quantitative chemical, and optical imaging of plant polymers.

s-SNOM in imaging mode. First investigation was performed using the imaging mode, where a monochromatic illumination (see Methods section for details on the illumination source) is chosen according to predetermined or known spectroscopic absorption features of the materials of interest. We first seek to obtain an image at a given wavenumber to obtain the spatial distribution of the corresponding polymeric component. By taking successive images of the same region at chosen wavenumbers, we aim to determine the colocalization of cellulose versus lignin, the two main structural polymers of PCW[48,49]. These wavenumbers were chosen based on a previous study using micro-fourier-transform infrared spectroscopy (FTIR), time-of-flight secondary ion mass spectrometry, and micro-Raman (see Supplementary Note 2, Supplementary Fig. 2) on exactly the same samples[15]. Figure 2 (extended data in Supplementary Note 3, Supplementary Fig. 3) shows the acquired s-SNOM images for a fresh Populus (FP) cross-section sample. The cell wall region of interest was selected at the intersection of three fibers to span the different parietal layers. Scanning electron microscopy, as well as AFM, were employed to image the region of interest, as shown in Supplementary Fig. 4 in Supplementary Note 4. Fig. 2a is shown here to emphasize that only limited information may be extracted from topographical images of rough samples. The corresponding reflectivity and absorption signals are recorded at 1063 cm^{-1}, and 1590 cm^{-1}, two absorption peaks that are highly selective to cellulose (Fig. 2c, d) and lignin (Fig. 2e, f), respectively (see Table 1). Although, the two reflectivity images in Fig. 2c, e evidence different optical contrasts such that a low reflectivity implies strong transmission and/or absorption, they are insufficient to be assigned to specific chemical components. In contrast, absorption is owing to the vibrational states of the molecules, provides the chemical distribution of the associated component with high resolution. In both absorption images, the contrast indicates the presence of higher quantities of the specific chemical constituent associated with the selected wavenumber. By comparing the two absorption images obtained at 1063 cm^{-1} (Fig. 2d) and 1590 cm^{-1} (Fig. 2f), both distribution and colocalization of the cellulose and lignin are revealed. For example, the black and green ovals indicate cellulose-rich and lignin-rich regions, respectively. In addition, Fig. 2 evidences a correlation, discussed thereafter, between cellulose versus lignin distribution (Fig. 2d, f) and the mechanical phase (Fig. 2b).

The advantages of the imaging mode are (1) its relatively easy implementation with only one wavelength used, (2) its fast acquisition, and (3) immediate highlighting of desired chemical components without post processing. The disadvantages are that the wavenumber of interest needs to be known precisely and the colocalization of different components requires successive scans of the same region. The spectroscopic mode discussed next allows overcoming these issues.

s-SNOM in spectroscopic mode. In complex materials such as plants, the vibrational frequencies of the different chemical bonds have been shown to strongly depend on the environmental variability, on the ordering of the molecules[50], and on the presence

Table 1 Main vibrational modes assignments.

Wavenumber [cm^{-1}]	Vibrational modes	Major assignments	Range	Refs.
1034	^{s}C-OH	Cellulose, ring	1029-1035	30,58
1048	^{s}C-OH	Xyloglucan, ring	1044-1045	31,67
1063	^{s}C-OH	Cellulose, ring	1053	58
1079	^{s}C-OH	Cellulose, C(3)-O(3)H ring	1058	58
1106	^{s}C-OH	Aliphatic Lignin, cellulose, hemicellulose	1106-1108	58,65,66
1159	^{as}C-O-C	Cellulose Xyloglucan	1158-1162	30,58,65,68
1246	^{s}C-O	Lignin (Guaiacyl units) linkage to CH_3 or ester Xylan acetyl and carboxyl	1231-1243	58,64,69
1263	^{s}C-O-C	Lignin	1261-1264	56,58
1316	^{w}C-H_2	Cellulose Xyloglucan	1316-1319	30,58,64,68
1377	^{b}C-H_2	Cellulose Xyloglucan	1365-1370	58,64,67
1463	^{b}C-H_3	Lignin, xylan in methoxy	1459-1470	58,66
1507	^{as}C=C	Lignin, aromatic ring	1505-1510	56,58,66
1590	^{s}C=C	Lignin aromatic ring	1595-1610	56,58,64
1611	^{s}C=C	Acetylated lignin		58
1651	C-O	Conjugated to C=O in acetylated lignin, cellulose, hemicellulose	1665-1666	58
1737	^{s}C=O	Xylan acetyl	1735-1740	30,56,58,64,69
1768, 1810, 1847	^{s}C=O	Acetylated lignin, cellulose, xyloglucan	1750-1850	56,68

s stretching, *b* bending, *as* asymetric stretching, *w* wagging.

of stress[51]. In wood tissues, absorption shifts as high as 10 cm^{-1} have been observed related to the cellulose chain[52–54]. C–O–H bending[53] at 1424 cm^{-1}, C–O stretching[54] at 1060 cm^{-1}, and 1160 cm^{-1} bands have been shown to decrease linearly with applied stress. Similarly, in Spruce wood, a 6 cm^{-1} shift to lower energy was reported for the C–O–C cellulose band at 1160 cm^{-1} under moist conditions with increasing relative humidity from 0 to 90%[54]. The presence of such discrepancies can cause uncertainties when using monochromatic imaging since any deviations in the spectral position of the peaks throughout the specimen, can lead to challenges in the interpretation of the data. To rule out such uncertainties, the spectroscopic mode was employed (Fig. 1, nano-FTIR[40,55]) using a broadband illumination s-SNOM and seek to acquire full IR absorption spectra at each selected position (i.e., mapping/line/point) on the sample. Note that measured spectroscopic signatures have been shown to be identical in nano-FTIR and conventional FTIR spectroscopy, hence allowing comparison with the existing vibrational database[40]. Cross-correlation of different absorption bands is then possible, providing more accurate identification of the local chemical composition and of possible band shifts. The absorption intensity depends on the changes in the dipole moment of the bond due to IR absorption that is proportional to the number of corresponding bonds. Therefore, it can be used to compare, quantitatively, different samples, if reference is made to the same absorption band. However, comparison across different bands may not be feasible as each band has its own vibrational sensitivity factor. Finally, colocalization of the different chemical components and their qualitative amounts can be extracted from the bands' relative intensities.

Here, the first hyperspectral data-cube images of PCW (Fig. 3) were obtained from both reflectivity (Fig. 3b) and absorption (Fig. 3c) measurements performed on an acetylated wood sample (EA sample). Both data sets were simultaneously acquired from a $1 \times 1\ \mu m^2$ area of a sample region. This region was chosen based on the analysis of the mechanical phase mapping (Fig. 3a) (see the section below) for its content of both lignin-rich (blue) and cellulose-rich (red) sub-regions. The resulting data cube contains the correlated spatial and spectral information for any selected planes or points at specific wavenumbers. Such intensity mapping $I(x,y,\nu)$ provides the absorption or reflectivity response, recorded at each pixel $(x,y)$of the mapping and for each wavenumber ν of the considered spectral range (see data processing in the Methods section). For example, Fig. 3d shows the spatial absorption distribution for one given wavenumber similarly to SNOM in imaging mode, whereas Fig. 3e displays the mapping of the whole spectrum $I(\nu)$ along the plane *P0* (gray in Fig. 3c) (extended data in Supplementary Note 5, Supplementary Fig. 5). Both reflectivity and absorption will be used further to extract and correlate the chemical distribution and the local optical properties in relation to the spatial location at the nanoscale.

Mechanical phase. As previously mentioned, further correlations can be established via phase imaging, which is classically acquired in tapping mode AFM. In this mode, the AFM cantilever is driven with periodic forcing. The phase lag between the driving signal of the cantilever and the output (readout) signal, representing the cantilever oscillations, depends on the cantilever–sample interaction force, and thus exhibits sensitivity to the sample material properties. By detecting the phase changes, one may therefore extract the variations in the mechanical properties of the sample surface. Thus, one obtains a mechanical phase image simultaneously to the topographic image. In particular, information on the viscoplasticity of the surface of the material may be obtained, as illustrated in Supplementary Fig. 6. The viscoplastic index, calculated from processing the quantitative force-volume mapping (indentation measurements by AFM, see Supplementary Note 6), reflects the ratio of elasticity and viscoplasticity behavior in relation to the chemical composition[43] and correlates nicely with the phase mapping. Although the absolute values of the phase shift depend on the experimental conditions and cantilever/tip properties and cannot be used to quantify the mechanical properties, a higher value of the phase lag indicates a higher viscosity of the materials. Here, we aim to correlate the mechanical phase signal with the optical signals, which can provide a unique nanoscale channel for linking the chemical composition to the optical and mechanical properties. The results are presented in Fig. 2 (extended data in Supplementary Note 3), where the topography and associated mechanical phase of the FP cross-section were recorded at the same location as reflectivity and absorption measurements in Fig. 2c–f. As observed, the topography (Fig. 2a) lacks physio-chemical characteristics that discriminate cellulose and lignin. In contrast, the mechanical phase (Fig. 2b) gives extraordinary features at the high spatial resolution but with no direct chemical identification of the different regions. By comparing Fig. 2b with Fig. 2d, f, we note that

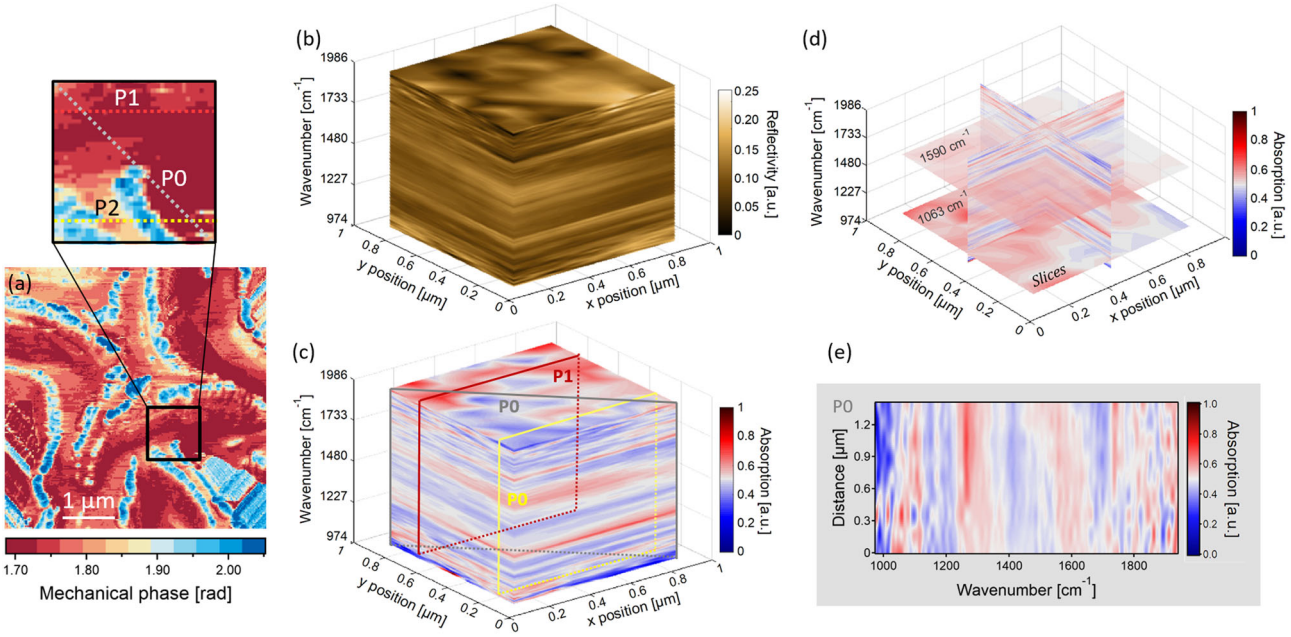

Fig. 3 Hyperspectral imaging of plant material. a Mechanical phase measurement of a $5 \times 5\,\mu m^2$ region of an EA sample. Hyperspectral mappings are carried out for the $1 \times 1\,\mu m^2$ region demarcated in **a**. Hyperspectral intensity data-cubes, $I(x,y,v)$ contain reflectivity (**b**) or absorption (**c**) information. **d** Slices were extracted from the absorption data cube at 1063 cm^{-1} and 1590 cm^{-1}, corresponding to the specific absorption of cellulose and lignin, respectively. **e** Spectral mapping of the absorption recorded for wavenumbers in the range 974–1986 cm^{-1} along plane *P0* (gray) (Planes *P1* and *P2* will be used further, see Fig. 4).

the mechanical phase strongly correlates with the absorption mappings. The cellulose regions are obtained for values of the mechanical phase ranging from 0.75 to 1 rad (regions in red Fig. 2b), whereas the range associated with lignin goes from 1.25 to 1.40 rad (regions in blue Fig. 2b) evidencing higher viscosity for lignin, in agreement with our previous work[16].

Having obtained correlative chemical, optical, and mechanical measurements, s-SNOM will be now employed to investigate the efficiency of a delignification process developed for biomass extraction. In addition, we will explore the changes in optical properties in relation to the chemical environment along the process by extracting the values of the cell wall local dielectric function, in their native form.

Investigation of a delignification process efficiency. A delignification process based on a three-step chemical extraction was proposed to remove lignin and hemicellulose (xylan and xyloglucan) from a young poplar tree (see method section for details) by increasing the solubility of all species through an acetylation process[15,56–58]. Here the study was performed in the second layer (S2) of the PCWs where xylan is the main hemicellulose, contributing to 20–40% of the biomass weight. In recent studies, it was shown that lignin does not show any direct interaction with cellulose surfaces[59], but instead extensive electrostatic interactions with flexible xylan and xyloglucan domains[60,61], and that hemicelluloses mediate the supramolecular connectivity between cellulose surfaces and lignin and the overall cell wall integrity[62]. The whole challenge in the delignification process is thus to diminish the interactions between the hemicellulose and, the cellulose and the lignin. Xylan interacts with cellulose and lignin through their backbones consisting in b-1,4 linked xylosyl residues through hydrogen bonding between the alcohol groups of the different species[61]. Substitution of these hydrogen bonds was shown to affect both the self-association of xylan and also its interaction with both lignin and cellulose[61].

The delignification protocol we used here aims at breaking the hydrogen bonds by substituting the alcohol groups with an ester, and hence increasing the solubility of both hemicellulose and lignin. To evaluate the efficiency of the process, four samples corresponding to each chemical step were prepared and analyzed: (FP) untreated reference fresh poplar sample, (EF) extractive-free sample, (EA) acetylated sample, and (AC) hydrolyzed sample. Prior to treatment, four successive 200 µm-thick cross-sections were obtained from the same stem region of the poplar tree and were considered similar in structure and composition.

Reflectivity (Fig. 4a–d) and absorption (Fig. 4e–h) measurements were first carried out on the secondary layer (S2) of the PCWs, which is rich in cellulose, hemicellulose, and lignin. For FP, EF, and AC samples, measurements were acquired along a line in the S2 region (Supplementary Note 7 in Supplementary Fig. 7). For the EA sample, data were extracted from the absorption data-cube (Fig. 3c) along the plane *P1* (red) for a cellulose-rich region (EA_C) and along the plane *P2* (yellow) for a lignin-rich region (EA_L), as previously identified from the mechanical phase image analysis (Fig. 3a). For each of the samples, absorption mappings (Fig. 4e–h) were acquired in the spectral range from 1030 cm^{-1} to 1855 cm^{-1}, i.e., covering most of the wood polymer's vibrational bands. To better compare the spectral data, averages of each of the mappings, shown in Fig. 4i, were normalized by the peak intensity of cellulose at 1063 cm^{-1}. This peak was chosen as it remains invariant over the extraction process[63]. From the FP sample mapping, the major absorption peaks, reported in Table 1, were identified for cellulose, lignin, and hemicellulose (xylan and xyloglucan). The bands above 1750 cm^{-1} were attributed to the fats and triglycerides. Absorption spectra of the EF sample show mainly the removal of the fats with no evidence of changes to the other spectral contributions, as expected. Subsequent esterification of EF, resulting in EA sample, induces however strong spectral changes related to the acetylation of lignin, xylan, xyloglucan, and cellulose. For the four species, the acetylation at the alcohol groups (–OH) results in shifts of the corresponding

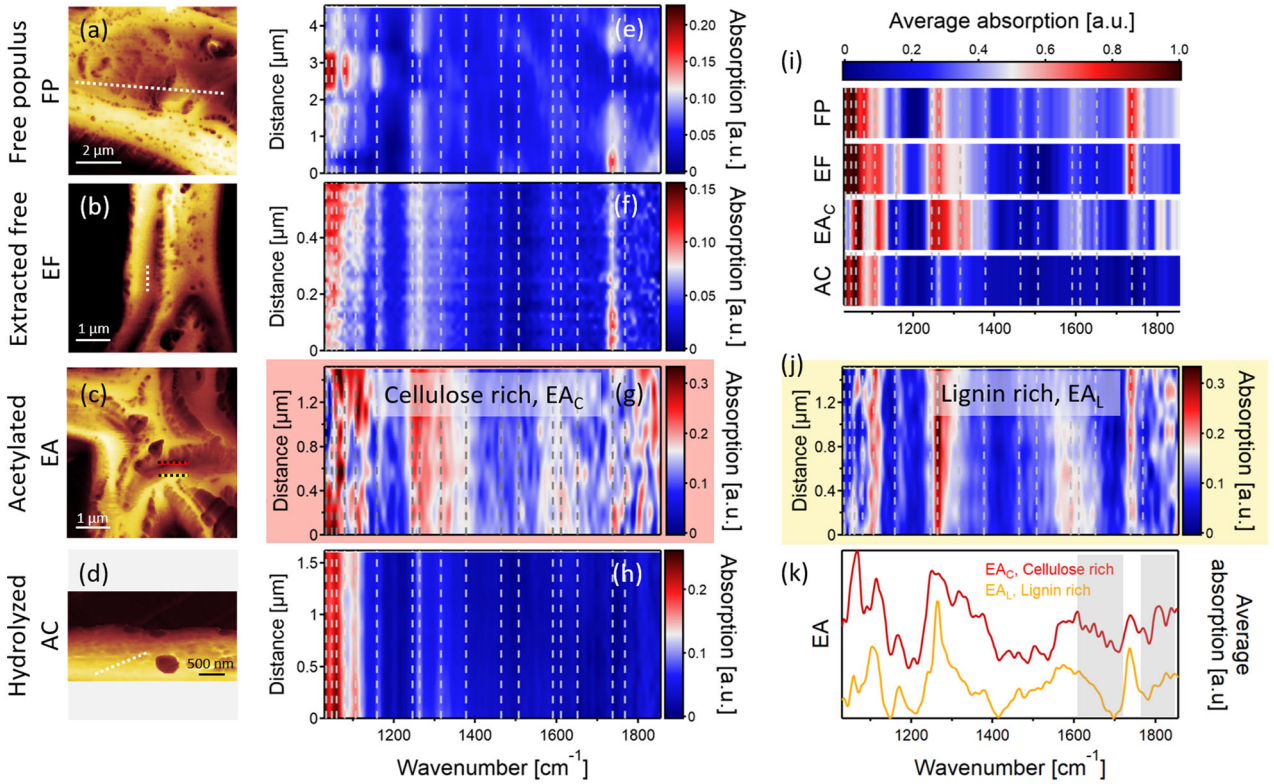

Fig. 4 Nanospectroscopic process monitoring via infrared absorption mapping. Reflectivity images (**a**–**d**) along the delignification process. The associated chemical compositions (**e**–**h**) extracted from the absorption images are mapped along the lines in the S2 region of the cell wall in **a**–**d**. For the EA sample, both cellulose-rich (EA_C, **g**, red) and lignin-rich (EA_L, **j**, yellow) regions were investigated (see Fig. 3c). **i** The average absorption for the FP, EF, EA_C, and AC samples was normalized by the intensity of the cellulose characteristic absorption band at 1059 cm^{-1}. In all mappings, the dotted lines indicate the wavenumbers of the absorption bands of interest corresponding to cellulose, hemicellulose, lignin, and fats, see Table 1. **k** Average absorption spectra obtained for the EA_C and EA_L regions. The bands in the range 1600–1720 cm^{-1} and above 1750 cm^{-1} (shaded areas) reflect the success of acetylation in the cellulose-rich regions (EA_C).

absorption bands (1034, 1048, 1059, 1079, and 1106 cm^{-1}) to higher energies in the range [1050–1140 cm^{-1}][31,63–67]. Also, an increase after esterification of the C–O absorption band of the guiacyl ring of lignin and of xylan carbonyl groups at 1246 cm^{-1}, suggests the acetylation of these groups has been successful[63,68,69]. In addition, the observation of new peaks at 1651 cm^{-1}, corresponding to C–O (conjugated with C=O in the ester), and at 1768, 1810, and 1843 cm^{-1}, corresponding to the C=0 of the ester confirms the success of the process[30,57,63]. Finally, the peaks corresponding to lignin aromatic skeleton vibrations at 1263 and 1507 cm^{-1} show no changes, indicating that the main structure of lignin was not damaged during esterification although partial removal of the xyloglucan and xylan was observed as shown by the net decrease of the intensities of the peaks at 1159, 1316, and 1737 cm^{-1}[30,57,63,68–70]. For the final AC samples, hydrolysis of EA samples in acidic conditions lead to the substitution of the ester groups to alcohol groups. The results of this process were the recovery of cellulose to its initial configuration (see –OH absorption bands in the range 1030 to 1110 cm^{-1}), and the extraction of lignin, xylan, and xyloglucan from the sample as supported by the significant decrease of their absorption bands. The remaining small amount of lignin, marked by the presence of the skeleton C–O–C stretching vibration at 1263 cm^{-1} (AC mapping), indicated however an incomplete extraction.

To better understand the origin of this remaining lignin, another region from the data cube (EA_L sample, Fig. 4j) was previously identified to be lignin-rich using mechanical phase imaging, in particular, in the S2 and S3 regions. Absorption mapping across this region (plane *P2* in Fig. 3a, c) shows high intensity at the aromatic skeleton vibrations at 1263 cm^{-1} and 1590 cm^{-1}, confirming lignin as the main compound. Note also the high intensity of the xylan C=O stretching band at 1737 cm^{-1}[69]. Interestingly, by comparing the average spectra obtained from the lignin-rich region (Fig. 4k, yellow curve) with the cellulose-rich (average spectrum Fig. 4k, red curve), one observes the absence of absorption bands in the spectral range above 1600 cm^{-1} (shaded zones in Fig. 4k), suggesting that acetylation of the lignin did not work efficiently. This may be conferred to lower solubility of the lignin in these regions in relation to its structure. This hypothesis is supported by previous work reporting that low and high molecular weight lignins exhibit different structural organizations, the latest displaying highly specific and stable association pattern[58,71]. Also, Ruel et al.[72,73] showed that the two most common lignin assemblies, the guaiacyl lignin (*g*-lignin), and the guaiacyl-syringyl lignins (*gs*-lignin) are distributed unequally in the PCW, *g*-lignin being concentrated in the inner S2 and S3 layers, and *gs*-lignin in the S1 and outer S2, hence suggesting that the lignin remaining after hydrolysis in the EA sample must be composed mostly of *g*-lignin. These results evidence that the lignin extraction protocol proposed here does not fully solve the problem of recalcitrance as it has an efficiency limited to low-weight lignin that is more soluble. Moreover, our results suggest that this lack of solubility of the *g*-lignin may not be due to a lack of solubility of the acetylated lignin but instead to a poor yield of the acetylation process. One way to increase this yield may require PCW pretreatment to destabilize the molecular association pattern of high-weight lignin such as mechanical grinding for

example. This clearly evidences the large interest of the presented technique for deeply understanding and feed-backing on wood treatments toward process optimization.

In the last part, we are finally questioning how the local optical properties of the PCWs are affected by the environmental variability at the nanoscale and how these properties can be modified by engineering the PCW, such as in the case of the delignification process.

In situ determination of nanoscale optical properties of PCW in their native form. *Index of refraction and extinction coefficient extraction*. The nanoscale optical properties of plant materials may not only be useful for fundamental light–matter interaction studies at the cellular and PCW levels, but also important in devising optical methods for measuring and monitoring the effect of chemical processing of biomass or toward biodegradable optical and electronic components. In the context of PCW, extracted or synthesized solutions for gel permeation chromatography is one of the main chemically driven techniques to measure the refractive index of the bulk wood polymers[74,75]. However, using interference microscopy[19], it was shown that the refractive index of the different polymers varies strongly with the considered PCW region, environment, and method of extraction, highlighting the importance of measuring the optical constants of such samples in their native form, hence requiring a lateral resolution at the nanometer scale.

In s-SNOM, the dielectric function ε of the sample may be calculated by Fourier transform of the detected scattered field $E_{\mathrm{Scat}} = E_{\mathrm{Scat}}(n_{\mathrm{probe}}, k_{\mathrm{probe}}, n_{\mathrm{sample}}, k_{\mathrm{sample}})$, where $\epsilon = (n + ik)^2$ denotes the complex dielectric function of the sample, and n and k the real and imaginary refractive indices, respectively[25,42]. The optical interaction between the probe and the sample depends on the complex dielectric function of the sample in the immediate proximity of the tip. For an incident field E_{Inc}, when the sample is in the nearfield of the probe apex, the resulting scattered field E_{Scat}, (Fig. 1), maybe written in the Fourier domain as:

$$E_{\mathrm{Scat}}(\omega) = \sigma_{\mathrm{Scat}}(\omega) E_{\mathrm{Inc}}(\omega), \tag{1}$$

where $\sigma_{\mathrm{Scat}}(\omega)$, the scattering coefficient[76–78] at frequency ω, is given, in the approximation of a low-absorbing and thick sample, by:

$$\sigma_{\mathrm{Scat}}(\omega) = \frac{\epsilon(\omega) - 1}{\epsilon(\omega) + 1}. \tag{2}$$

In the s-SNOM detection scheme of the Neaspec system, the light backscattered from the metallic tip is recorded through a Michelson interferometer, in which the sample-tip assembly is contained in one arm[79–81]. Using such asymmetric interferometric detection, amplitude $A(\omega)$ and phase $\varphi(\omega)$ electric field components of the backscattered light are acquired simultaneously. The scattering coefficient is then expressed as:

$$\sigma_{\mathrm{Scat}}(\omega) = A(\omega) e^{i\varphi(\omega)} \tag{3}$$

For polymeric/organic materials, the measured reflection $r(\omega)$ and absorption $a(\omega)$ are related to the real and imaginary parts of the scattering coefficient[82–84] and expressed as:

$$r(\omega) = \Re[\sigma_{\mathrm{Scat}}(\omega)] = A(\omega)\cos[\varphi(\omega)] \tag{4}$$

and

$$a(\omega) = \Im[\sigma_{\mathrm{Scat}}(\omega)] = A(\omega)\sin[\varphi(\omega)] \tag{5}$$

The refractive indices (n, k) of the samples are then extracted using Eqs. 2, 4, and 5 using iterative calculation[85].

Environmental variability and spectral distribution of n and k at the nanoscale. The (n, k) extraction was obtained at each position and wavenumber from the data cube of the EA sample (Fig. 3). Fig. 5 shows the (n, k) mappings at four absorption bands: (1034 and 1063 cm^{-1}), highly selective to cellulose, and (1263 and 1590 cm^{-1}) specific to lignin (see Table 1). Within each of the mappings, the values of n and k are seen to vary significantly with n changing from 1.1 to 1.3, and k from 0.1 to 0.22 for cellulose band, and from 0.15 to 0.35 for the lignin absorption band. Such changes are indicative of the degree to which the local environment modifies the optical properties at the nanoscale. However, although the n-mappings (Fig. 5a–d) are very similar for the four considered wavenumbers and do not seem to be related to the chemical distribution of the two polymers, the k mappings in contrast show very specific distributions whether one considers the wavenumbers corresponding to the cellulose (Fig. 5e, f) or the lignin (Fig. 5g, h) absorption bands. This observation confirms the correlation between the extinction coefficient and the chemical distribution. Moreover, the most intense values of k (red regions) for the lignin absorption bands (Fig. 5g, h) match perfectly with the inner S2–S3 layers containing dense and high molecular weight lignin as discussed previously and identified by the mechanical phase imaging in Figs. 3a and 2b (blue regions). Similarly, the high values of k in the mappings obtained at the cellulose bands correspond to cellulose-rich regions. Although individual values of n have been previously reported for bulk plant material, using extractive chemical methods in the visible range, here, for the first time, we are reporting the n and k distribution, for both cellulose and lignin within PCW in their native form, at their IR absorption bands.

Analyzing further the n and k mappings, two positions may be selected for being cellulose-rich (C, pink dot) and lignin-rich (L, yellow dot), as marked in Fig. 5. The corresponding $(n, k)_{\mathrm{cellulose}}$ and $(n, k)_{\mathrm{lignin}}$ dispersions are plotted over the wavenumber range in Fig. 5i, j, respectively. Within this spectral range, the $n_{\mathrm{cellulose}}$ spans from 1.06 to 1.19 and the $k_{\mathrm{cellulose}}$ from 0.08 to 0.29, whereas the n_{lignin} ranges from 1.15 to 1.40 and the k_{lignin} from 0.05 to 0.4. These data evidence the n and k variability over the whole spectral region as a response to local polymer distribution. In the absence of literary references, we validated the presented method and the reported values of n and k by bulk FTIR measurements (see Supplementary Note 8, Supplementary Fig. 8). Note that at the macroscopic scale, the reflectivity signal and consequently the refractive index appear noisy, in part due to interfering effects and roughness induced scattering.

These results illustrate the fact that the optical constants are highly dependent on the local composition at the nanoscale and demonstrate the correlation between the chemical information, the optical and mechanical properties.

n and k variations during delignification process. To investigate the chemical changes in the PCWs as a result of the delignification treatment, refractive index and extinction coefficients were determined in the spectral range [1030–1855 cm^{-1}] for each sample, i.e., FP, EF, EA, and AC samples in the same S2 regions as discussed in the delignification section. For each sample, the average values of n (gray) and k (red) obtained over the different measured positions for the whole spectral range are shown in Supplementary Fig. 9 in Supplementary Note 9. The corresponding shaded areas are the standard deviations. Fig. 6 focuses the analysis on the initial untreated FP and final holopulped AC samples. For the FP sample, the n and k values vary from 1.198 to 1.333 and from 0.018 to 0.164, respectively, and for the AC sample from 1.173 to 1.493 and from 0.043 to 0.336, respectively, showing the evolution of both optical constants over the delignification process. Also, the large standard deviations in the FP sample (Fig. 6a), 0.040 ± 0.006 and 0.025 ±

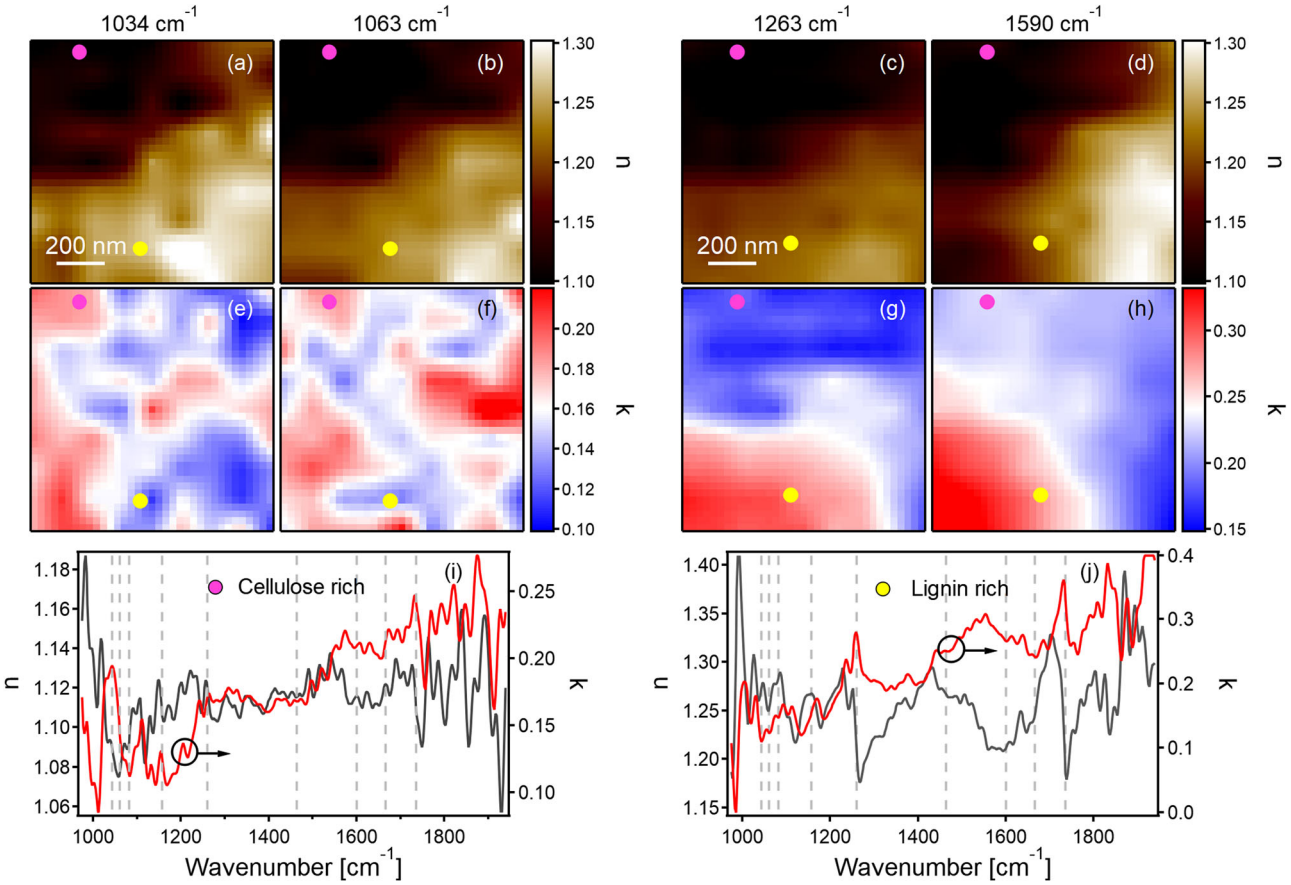

Fig. 5 In situ high-resolution determination of nanoscale optical properties of PCW in their native form. Measurement of the complex index of refraction $n+ik$ for cellulose (**a**–**b**, **e**–**f**, **i**) and lignin (**c**–**d**, **g**–**h**, **j**), over a $1 \times 1\,\mu m^2$ region, is calculated from the reflectivity and absorption hyperspectral measurements of EA sample by selecting the specific slices (Fig. 3). Images **a**–**b** and **e**–**f** display the indices mappings at 1034 and 1063 cm^{-1} absorption peaks for cellulose. **c**–**d** and **g**–**h** show the lignin optical response by targeting specific peaks at 1263 and 1590 cm^{-1}. **i** and **j** display the spectral dispersion of $(n, k)_{cellulose}$ and $(n, k)_{lignin}$, respectively. These spectra are evaluated at the points marked in the n and k mappings (**a**–**h**) as C (Pink) for a cellulose-rich location and L (Yellow) for a lignin-rich location.

0.009 for n and k, respectively, reflect the variability of the chemical environment at each position and hence show the effect of this environment on the optical constants. In the AC sample in contrast (Fig. 6b), the standard deviation is much smaller, 0.011 ± 0.005 and 0.010 ± 0.004 for n and k, respectively, highlighting the uniformity of the chemical environment in agreement with a nearly cellulose-only made material, as discussed earlier. The AC spectra hence reflect the n and k spectral distribution of nearly pure cellulose in their native form and the final values of $n = 0.226$ and $k = 0.311$ obtained for a wavenumber of 1058 cm^{-1} (Fig. 6b), i.e., corresponding to a specific absorption band of cellulose, are hence the signature of delignified PCW in their native form.

Conclusion

The presented results amount to a demonstration of the complementarity of multimodal s-SNOM for exploring the correlative chemical and optical properties of wood, in general, and for process monitoring, in particular, at a spatial resolution of 20 nm. Here, the analysis of the proposed delignification process enabled to allow observation of different lignin acetylation yields in relation to their structure and location in the PCW. Our results suggest that increasing the yield of delignification may require additional PCW pretreatments such as, for example, a mechanical grinding, to destabilize the molecular association pattern of high-weight lignin. Such monitoring of the specific process of delignification at the nanometer scale clearly suggests that the presented measurements can apply to a larger class of biomass pretreatments and could be extended to other complexed material processes.

We also provided, to the best of our knowledge, the first optical indices (n and k) mappings of PCW at the nanoscale in the IR range evidencing a strong correlation of these indices with the chemical composition, the dispersion of their values over different regions reflecting the environmental variability of the sample. These results, establishing a correlation between the chemical distribution and the optical properties suggest new modalities in plant metrology. Furthermore, the acquisition of the mechanical phase by the microcantilever, serving as the s-SNOM probe, can allow extending this correlation to some mechanical properties such as viscoelasticity. We suggest this technique can uniquely facilitate not only the understanding of the wood morphogenesis and associated physical and chemical properties but also the control of the engineering of wood. As a sustainable resource, wood is becoming a material of choice not only for the paper market or for the biofuel industry, an expanding market, but also for the development of smart building components, with the engineering of new plant-based (meta-)materials. High precision control of the mechanical and optical properties of wood production will be a major concern, for example, in the emerging field of additive manufacturing, where the presented nanometrology can be a key capability.

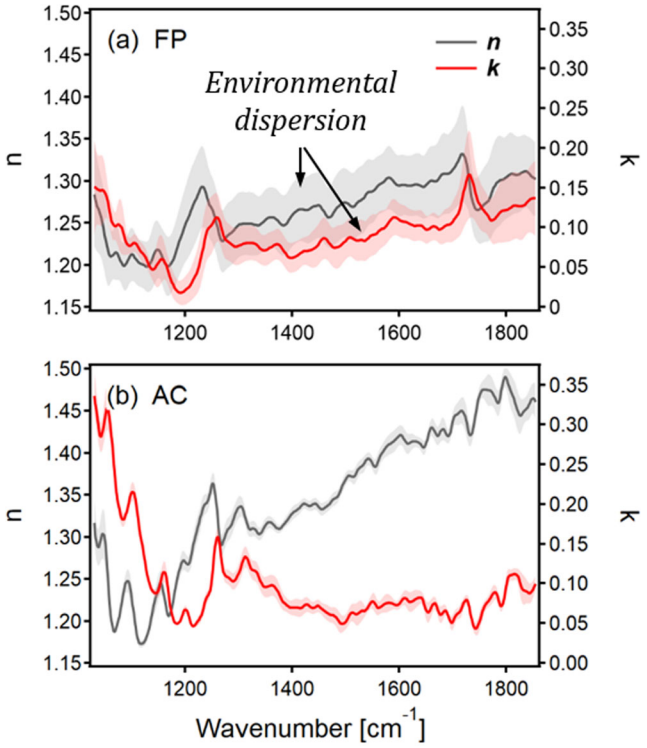

Fig. 6 Environmental chemical variability evidenced through the optical dispersion. Determination of the average optical properties of plant material via measurement of the complex index of refraction $n+ik$. The average refractive index n and extinction coefficients k for **a** untreated FP and **b** holopulped AC samples were determined from the amplitude and phase of the scattering nearfield recorded along a line. The corresponding shaded areas are the standard deviations which reflect the environmental dispersions of n and k.

Methods

Nano-FTIR s-SNOM (NEASPEAC GmbH). The used spectral range spans from 1030 cm^{-1} to 1855 cm^{-1} in order to access the main specific IR absorption bands of cellulose and lignin. For the imaging mode, we used a continuous quantum cascade laser water-cooled and tunable from 850 cm^{-1} to 2500 cm^{-1} with an output dimmed down to 1 mW at each wavelength to avoid sample damage. For the nano-FTIR measurements, a broadband laser, tunable from 650 cm^{-1} to 2150 cm^{-1}, pulsed at a repetition rate of 80 MHz with a 1 mW output power was used. Note that a ~700 cm^{-1} spectral region can be covered at once with such broadband source. The second harmonic demodulation detection of the optical signal is used to eliminate the far-field background while keeping enough optical signal contrast. Indeed, the polymeric wood constituents classically have a similar optical response implying low optical contrast. Commercial tips, Arrow-NCPt (NanoWorld, Switzerland), coated with Platinum-Iridium5 (Pt-Ir5), with a radius of ~20 nm, were utilized in the whole study. The presented nano-FTIR results have a spatial resolution ranging from 20 nm to 100 nm for the spectroscopic measurements and 20 nm for the imaging measurements.

Plant material[86]. For 6 months, *Populus deltoides × nigra (DN34)* hybrids were cultivated under fixed greenhouses conditions such as 16 hours of light per day, a humidity level between 30% and 60%, and automatically watered four times a day at a fixed hour. The plants were grown in soil (Sun-Gro Sunshine Mix #4) mixed with fertilizer (Miracle Gro 20-20-20). After the first 6 months of growth, the full stems were cut and directly frozen at −20 °C. Note that the Populus deltoides stump used here was harvested during its juvenile phase.

Sample preparation. FP samples were obtained from young poplar (*Populus deltoides × nigra (DN34)*) stem by freezing then sectioning successive thin cross-sections (20 µm in thickness) in the same region of the stem with a cryotome using a disposable blade that was free of any lubricant. DP samples were obtained after chemical treatment of the freshly cut FP cross-sections according to the following protocol: extractives were removed by refluxing FP samples with dichloromethane (CH_2CL_2, an organic solvent) for 6–12 h resulting in EF samples. Lignin was subsequently removed after treating the EF samples with glacial acetic acid (CH_3COOH) and sodium chlorite ($NaClO_2$) at 70 °C for 2 h resulting in acetylated (EA) samples. EA samples were then rinsed twice with DI water. Final lignin and hemicellulose extraction was performed using 2.5 M hydrogen chloride (HCl) at 100°C for 4 h resulting in hydrolyzed (AC) samples. AC samples were then rinsed with DI water. Note that this process results in cellulose-rich samples with traces of lignin and hemicellulose[15,16]. To maintain the structural integrity of the PCWs, all samples were stored and dried between glass slides. The final sample global roughness was ~2 µm and local roughness ~20 nm.

Data processing. Color map representations of series of absorption spectra recorded along a line (1D) were processed as follows: a baseline corresponding to the phase correction was removed from each spectrum. A binomial smoothing was then applied to the whole map. Maps were finally normalized between 0 and 1 for the lowest and the highest values of the absorption respectively. For a 2D region, hyperspectral representation is obtained by stacking the resulting color maps obtained for each scanned wavenumber.

Data availability

The data that support the findings of this study are available from the corresponding author upon reasonable request.

Received: 3 September 2020; Accepted: 17 May 2021;
Published online: 09 June 2021

References

1. Siro, I. & Plackett, D. Microfibrillated cellulose and new nanocomposite materials: a review. *Cellulose* **17**, 459–494 (2010).
2. Shinde, S. D. et al. Recent advances in understanding the pseudo-lignin formation in a lignocellulosic biorefinery. *Green Chemistry* **20**, 2192–2205 (2018).
3. Råberg, U. & Hafrén, J. Biodegradation and appearance of plastic treated solid wood. *Int. Biodeterior. Biodegr.* **62**, 210–213 (2008).
4. Chen, M. J. et al. Homogeneous transesterification of sugar cane bagasse toward sustainable plastics. *ACS Sustainable Chem. Eng.* **5**, 360–366 (2017).
5. Zhu, H. L. et al. Transparent nanopaper with tailored optical properties. *Nanoscale* **5**, 3787 (2013).
6. Wu, J. M. et al. Impact of delignification on morphological, optical and mechanical properties of transparent wood. *Compos. Part A Appl. Sci. Manuf.* **117**, 324–331 (2019).
7. Kubovský, I. et al. Structural changes of oak wood main components caused by thermal modification. *Polymers (Basel)* **12**, 485 (2020).
8. Kučerová, V. et al. Changes in chemical and optical properties of silver fir (Abies alba L.) wood due to thermal treatment. *J. Wood Sci.* **65**, 21 (2019).
9. Li, T. et al. Anisotropic, lightweight, strong, and super thermally insulating nanowood with naturally aligned nanocellulose. *Sci. Adv.* **4**, eaar3724 (2018).
10. Zhang, N. et al. Improvement of mechanical, humidity resistance and thermal properties of heat-treated rubber wood by impregnation of SiO2 precursor. *Sci. Rep.* **9**, 982 (2019).
11. Papadopoulos, A. N. et al. Nanomaterials and chemical modifications for enhanced key wood properties: a review. *Nanomaterials* **9**, 607 (2019).
12. Sawada, D. et al. Tension wood structure and morphology conducive for better enzymatic digestion. *Biotechnol. Biofuels* **11**, 44 (2018).
13. Gierlinger, N. New insights into plant cell walls by vibrational microspectroscopy. *Appl. Spectrosc. Rev.* **53**, 517–551 (2018).
14. Goudenhooft, C. et al. investigation of the mechanical properties of flax cell walls during plant development: the relation between performance and cell wall structure. *Fibers* **6**, 6 (2018).
15. Farahi, R. H. et al. Plasticity, elasticity, and adhesion energy of plant cell walls: nanometrology of lignin loss using atomic force microscopy. *Sci. Rep.* **7**, 1–11 (2017).
16. Charrier, A. M. et al. Nanometrology of biomass for bioenergy: the role of atomic force microscopy and spectroscopy in plant cell characterization. *Front. Energy Res.* **6**, 11 (2018).
17. Lereu, A. L. et al. Nanomechanics and raman spectroscopy of in situ native carbohydrate storage granules for enhancing starch quality and lignocellulosic biomass production. *ACS Omega* **5**, 2594–2602 (2020).
18. Orelma, H. et al. Optical cellulose fiber made from regenerated cellulose and cellulose acetate for water sensor applications. *Cellulose* **27**, 1543–1553 (2020).
19. Donaldson, L. A. Critical assessment of interference microscopy as a technique for measuring lignin distribution in cell walls. *New Zeal. J. For. Sci.* **15**, 349–360 (1985).
20. Micic, M. et al. Study of the lignin model compound supramolecular structure by combination of near-field scanning optical microscopy and atomic force microscopy. *Colloids Surf. B Biointerfaces* **34**, 33–40 (2004).
21. Radotić, K. et al. New insights into the structural organization of the plant polymer lignin. *Ann. N. Y. Acad. Sci.* **1048**, 215–229 (2005).

22. Yarbrough, J. M. et al. Plant cell wall characterization using scanning probe microscopy techniques. *Biotechnol. Biofuels* **2**, 17 (2009).
23. Keplinger, T. et al. A zoom into the nanoscale texture of secondary cell walls. *Plant Methods* **10**, 1 (2014).
24. Rygula, A. et al. Raman, AFM and SNOM high resolution imaging of carotene crystals in a model carrot cell system. *Spectrochim. Acta Part A Mol. Biomol. Spectrosc.* **197**, 47–55 (2018).
25. Sun, X. H. et al. Using spectra analysis and scanning near-field optical microscopy to study Eu doped polymer fiber. *Optics Communications* **208**, 111–115 (2002).
26. Rosu, D. et al. FTIR and color change of the modified wood as a result of artificial light irradiation. *J. Photochem. Photobiol. B Biol.* **99**, 144–149 (2010).
27. Konagaya, K. et al. Optical properties of drying wood studied by time-resolved near-infrared spectroscopy. *Opt. Express* **24**, 9561 (2016).
28. Kristensen, J. B. et al. Cell wall structural changes in wheat straw pretreated for bioethanol production. *Biotechnol. Biofuels* **1**, 5 (2008).
29. Li, X. et al. Quantitative visualization of lignocellulose components in transverse sections of moso bamboo based on FTIR macro- and micro-spectroscopy coupled with chemometrics. *Biotechnol. Biofuels* **11**, 263 (2018).
30. Xu, F. et al. Qualitative and quantitative analysis of lignocellulosic biomass using infrared techniques: a mini-review. *Appl. Energy* **104**, 801–809 (2013).
31. Raspolli Galletti, A. M. et al. Midinfrared FT-IR as a tool for monitoring herbaceous biomass composition and its conversion to furfural. *J. Spectrosc.* **2015**, 1–12 (2015).
32. Traoré, M. et al. Application of FTIR spectroscopy to the characterization of archeological wood. *Spectrochim. Acta Part A Mol. Biomol. Spectrosc.* **153**, 63–70 (2016).
33. Schmidt, M. et al. Label-free in situ imaging of lignification in the cell wall of low lignin transgenic Populus trichocarpa. *Planta* **230**, 589–597 (2009).
34. Zeng, Y. et al. Imaging lignin-downregulated alfalfa using coherent anti-stokes raman scattering microscopy. *BioEnergy Res.* **3**, 272–277 (2010).
35. Gierlinger, N. & Schwanninger, M. Chemical imaging of poplar wood cell walls by confocal microscopy. *Plant Physiol.* **140**, 1246–1254 (2010).
36. Agarwal, U. P. An overview of Raman spectroscopy as applied to lignocellulosic materials. In *Advances in Lignocellulosics Characterization*. (ed. Argyropoulos, E.) Ch. 9, 201–225 (TAPPI Press, 1999).
37. Agarwal, U. P. Raman imaging to investigate ultrastructure and composition of plant cell walls: distribution of lignin and cellulose in black spruce wood (Picea mariana). *Planta* **224**, 1141–1153 (2006).
38. Tetard, L. et al. Opto-nanomechanical spectroscopic material characterization. *Nat. Nanotechnol.* **10**, 870–877 (2015).
39. Bek, A. et al. Apertureless scanning near field optical microscope with sub-10nm resolution. *Rev. Sci. Instrum.* **77**, 043703 (2006).
40. Huth, F. et al. Nano-FTIR absorption spectroscopy of molecular fingerprints at 20 nm spatial resolution. *Nano Lett.* **12**, 3973–3978 (2012).
41. Bouillard, J.-S. G. et al. Near-field hyperspectral optical imaging. *ChemPhysChem* **15**, 619–629 (2014).
42. Govyadinov, A. A. et al. Quantitative measurement of local infrared absorption and dielectric function with tip-enhanced near-field microscopy. *J. Phys. Chem. Lett.* **4**, 1526–1531 (2013).
43. Scott, W. Use of phase imaging in atomic force microscopy for measurement of viscoelastic contrast in polymer nanocomposites and molecularly thick lubricant films. *Ultramicroscopy* **97**, 151–169 (2003).
44. Mastel, S. et al. Understanding the image contrast of material boundaries in IR nanoscopy reaching 5 nm spatial resolution. *ACS Photonics* **5**, 3372–3378 (2018).
45. Ocelic, N. et al. Pseudoheterodyne detection for background-free near-field spectroscopy. *App. Phys. Lett.* **89**, 101124 (2006).
46. Moreno, C. et al. Phase imaging and detection in pseudo-heterodyne scattering scanning near-field optical microscopy measurements. *App. Opt.* **56**, 1037–1045 (2017).
47. Pereira, L. et al. Infrared nanospectroscopy reveals the chemical nature of pit membranes in water-conducting cells of the plant xylem. *Plant Physiol.* **177**, 1629–1638 (2018).
48. Bergander, A. & Salmén, L. Cell wall properties and their effects on the mechanical properties of fibers. *J. Mater. Sci.* **37**, 151–156 (2002).
49. Yamamoto, H. et al. Origin of the biomechanical properties of wood related to the fine structure of the multi-layered cell wall. *J. Biomech. Eng.* **124**, 432–440 (2002).
50. Westermeier, C. et al. Sub-micron phase coexistence in small-molecule organic thin films revealed by infrared nano-imaging. *Nat. Commun.* **5**, 4101 (2014).
51. Huber, A. J. et al. Infrared nanoscopy of strained semiconductors. *Nat. Nanotechnol.* **4**, 153–157 (2009).
52. Cintrón, M. & Hinchliffe, D. FT-IR Examination of the development of secondary cell wall in cotton fibers. *Fibers* **3**, 30–40 (2015).
53. Schwanninger, M. et al. Determination of lignin content in norway spruce wood by fourier transformed near infrared spectroscopy and partial least squares regression. Part 1: Wavenumber selection and evaluation of the selected range. *J. Near Infrared Spectrosc.* **19**, 319–329 (2011).
54. Salmén, L. & Bergström, E. Cellulose structural arrangement in relation to spectral changes in tensile loading FTIR. *Cellulose* **16**, 975–982 (2009).
55. Brehm, M. et al. Spectroscopic near-field microscopy using frequency combs in the mid-infrared. *Opt. Express* **14**, 11222 (2006).
56. Pawar, P. M.-A. et al. Acetylation of woody lignocellulose: significance and regulation. *Front. Plant Sci.* **4**, 118 (2013).
57. Zhao, X. et al. Efficient solid-phase synthesis of acetylated lignin and a comparison of the properties of different modified lignins. *J. Appl. Polym. Sci.* **134**, 44276 (2017).
58. Asikkala, J. et al. Accurate and reproducible determination of lignin molar mass by acetobromination. *J. Agric. Food Chem.* **60**, 8968–8973 (2012).
59. Iwata, T. et al. Affinity of hemicellulose for cellulose produced by Acetobacter xylinum. *Cellulose* **5**, 215–228 (1998).
60. Kang, X. et al. Lignin-polysaccharide interactions in plant secondary cell walls revealed by solid-state NMR. *Nat. Commun.* **10**, 347 (2019).
61. Terrett, O. M. et al. Molecular architecture of softwood revealed by solid-state NMR. *Nat. Commun.* **10**, 4978 (2019).
62. Berglund, J. et al. Wood hemicelluloses exert distinct biomechanical contributions to cellulose fibrillar networks. *Nat. Commun.* **11**, 4692 (2020).
63. Popescu, C.-M. et al. Structural analysis of photodegraded lime wood by means of FT-IR and 2D IR correlation spectroscopy. *Int. J. Biol. Macromol.* **48**, 667–675 (2011).
64. Shi, J. et al. FTIR studies of the changes in wood chemistry from wood forming tissue under inclined treatment. *Energy Procedia* **16**, 758–762 (2012).
65. Chen, H. et al. Qualitative and quantitative analysis of wood samples by Fourier transform infrared spectroscopy and multivariate analysis. *Carbohydr. Polym.* **82**, 772–778 (2010).
66. Yang, H. et al. Characteristics of hemicellulose, cellulose and lignin pyrolysis. *Fuel* **86**, 1781–1788 (2007).
67. Szymanska-Chargot, M. & Zdunek, A. Use of ft-ir spectra and pca to the bulk characterization of cellwall residues of fruits and vegetables along a fraction process. *Food Biophysics* **8**, 29–42 (2013).
68. Chen, C. et al. Elemental analysis, chemical composition, cellulose crystallinity, and FT-IR spectra of Toona sinensis wood. *Monatshefte für Chemie—Chem. Mon.* **145**, 175–185 (2014).
69. Cuello, C. et al. Microspectroscopy brings a novel insight into the study of cell wall chemistry at the cellular level. *Front. Plant Sci.* **11**, 105 (2020).
70. Musule, R. et al. Chemical composition of lignocellulosic biomass in the wood of Abies religiosa across an altitudinal gradient. *J. Wood Sci.* **62**, 537–547 (2016).
71. Cathala, B. et al. Association behaviour of lignins and lignin model compounds studied by multidetector size-exclusion chromatography. *J. Chromatogr. A* **1020**, 229–239 (2003).
72. Ruel, K. et al. The wood cell wall at the ultrastructural scale-formation and topochemical organization. *Maderas. Cienc. y Tecnol.* **8**, 107–116 (2006).
73. Ruel, K. et al. Impact of CCR1 silencing on the assembly of lignified secondary walls in Arabidopsis thaliana. *New Phytol.* **184**, 99–113 (2009).
74. Minor, J. L. Gel-permeation chromatography of polymers from wood. *J. Liquid Chromatogr.* **2**, 309–318 (1979).
75. Cooper, A. R. & Matzinger, D. P. Aqueous gel permeation chromatography: the effect of solvent ionic strength. *J. Appl. Polym. Sci.* **23**, 419–427 (1979).
76. Knoll, B. & Keilmann, F. Near-field probing of vibrational absorption for chemical microscopy. *Nature* **399**, 134–137 (1999).
77. Hillenbrand, R. & Keilmann, F. Complex optical constants on a subwavelength scale. *Phys. Rev. Lett.* **85**, 3029–3032 (2000).
78. Cvitkovic, A. et al. Analytical model for quantitative prediction of material contrasts in scattering-type near-field optical microscopy. *Opt. Express* **15**, 8550 (2007).
79. Qazilbash, M. M. et al. Mott transition in VO2 revealed by infrared spectroscopy and nano-imaging. *Science* **318**, 1750–1753 (2007).
80. Amarie, S. et al. Mid-infrared near-field spectroscopy. *Opt. Express* **17**, 21794 (2009).
81. Amarie, S. & Keilmann, F. Broadband-infrared assessment of phonon resonance in scattering-type near-field microscopy. *Phys. Rev. B* **83**, 045404 (2011).
82. Taubner, T. et al. Nanoscale polymer recognition by spectral signature in scattering infrared near-field microscopy. *Appl. Phys. Lett.* **85**, 5064–5066 (2004).
83. Paulite, M. et al. Imaging secondary structure of individual amyloid fibrils of a β 2 -microglobulin fragment using near-field infrared spectroscopy. *J. Am. Chem. Soc.* **133**, 7376–7383 (2011).
84. Stiegler, J. M. et al. Nanoscale infrared absorption spectroscopy of individual nanoparticles enabled by scattering-type near-field microscopy. *ACS Nano* **5**, 6494–6499 (2011).
85. Sun, J. & Lucyszyn, S. Extracting complex dielectric properties from reflection-transmission mode spectroscopy. *IEEE Access* **6**, 8302–8321 (2018).

86. Seokwon, J. et al. Surface characterization of dilute acid pretreated populus deltoides by ToF-SIMS. *Energy Fuels* **24**, 1347–1357 (2010).

Acknowledgements

This work was sponsored by the A*MIDEX foundation on the Innovation and Emergence AAP2017 (project no.: A-M-AAP-EI-17-10-170224-18.04-CHARRIER-E) and the CNRS through the PICS program 2019. The authors want to acknowledge the Neaspec GmbH, Munich Germany for their help in experimental measurements and for their fruitful discussions and J. Le Rouzo from the IM2NP-Marseille-France for FTIR measurements. A.P. acknowledges the BioEnergy Science Center (BESC) of the Oak Ridge National Laboratory (ORNL). ORNL is managed by UT-Battelle, LLC, for the US DOE under contract DE-AC05- 00OR22725.

Author contributions

A.L.L. and A. P. proposed and designed the study. A.L.L. led the s-SNOM imaging, the nano-FTIR, and FTIR experiments. A.M.C. and A.L.L. analyzed the data. A.P. provides wood cross-section dedicated to scanning probe imaging. A.N. performed the phase experiments. P.S. and A.L.L. performed the nano-FTIR imaging. All authors interpreted the results, wrote and approved the manuscript.

Competing interests

The authors declare no competing interests.

Additional information

Supplementary information The online version contains supplementary material available at https://doi.org/10.1038/s43246-021-00166-7.

Correspondence and requests for materials should be addressed to A.L.L.

Peer review information Communications Materials thanks the anonymous reviewers for their contribution to the peer review of this work. Primary handling editor: Aldo Isidori. Peer reviewer reports are available.

Reprints and permission information is available at http://www.nature.com/reprints

Publisher's note Springer Nature remains neutral with regard to jurisdictional claims in published maps and institutional affiliations.

Open Access This article is licensed under a Creative Commons Attribution 4.0 International License, which permits use, sharing, adaptation, distribution and reproduction in any medium or format, as long as you give appropriate credit to the original author(s) and the source, provide a link to the Creative Commons license, and indicate if changes were made. The images or other third party material in this article are included in the article's Creative Commons license, unless indicated otherwise in a credit line to the material. If material is not included in the article's Creative Commons license and your intended use is not permitted by statutory regulation or exceeds the permitted use, you will need to obtain permission directly from the copyright holder. To view a copy of this license, visit http://creativecommons.org/licenses/by/4.0/.

© The Author(s) 2021